Materials Advances

ROYAL SOCIETY OF CHEMISTRY

PAPER

View Article Online
View Journal | View Issue

Cite this: *Mater. Adv.*, 2022, 3, 6584

Colour tunable cool pigments based on $TiZn_2O_4$ inverse spinels†

Deepak Joshy,[a] Chamundi P. Jijil,[a] Sheethu Jose,[b] Yahya A. Ismail [a] and Pradeepan Periyat *[c]

Received 16th May 2022,
Accepted 13th July 2022

DOI: 10.1039/d2ma00537a

rsc.li/materials-advances

A new class of near-infrared (NIR) reflecting yellow and orange cool pigments based on $TiZn_2O_4$ inverse spinels were synthesized. The colour tuning in pure $TiZn_2O_4$ was made possible by the substitution of octahedral Zn^{2+} ions by Cu^{2+} and Fe^{3+} ions separately. By the incorporation of Cu^{2+} and Fe^{3+} ions into the inverse spinel lattice in varying amounts, a series of pigment compositions having colours ranging from greenish-yellow to reddish-brown was obtained. The developed pigments exhibited moderate to high NIR reflectance ranging from 47.61 to 87.81%. The $TiZn_2O_4$ based NIR reflecting pigment provided an interior 4.8 °C cooler than an uncoated roofed interior. Cu^{2+} and Fe^{3+} doped $TiZn_2O_4$ systems were found to be highly stable and eco-friendly cool pigment candidates capable of achieving better thermal conditioning and impressive energy conservation.

Introduction

Colour plays a crucial role in conveying information, creating memories, determining moods, and even in decision making. In such a way, inorganic pigments capable of imparting colours also have an effect on us. There are a wide range of inorganic pigments available in the market spanning over a broad range of colours.[1,2] The investigations for more attractive and affordable pigments with better characteristics are still on. The development of environmentally benign inorganic pigments is one of the prime objectives of pigment manufacturers. The presence of elements such as Cd, Cr and Pb in pigment compositions is discouraged nowadays.[3,4] Lead tin oxide ($PbSnO_3$), cadmium sulfide (CdS), nickel titanate ($NiTiO_3$), Al_2O_3:Cr^{3+} (corundum), cadmium red (CdS:CdSe), *etc.* are some of the conventional inorganic pigments in the yellow-orange-red colour range in use.[5–9] The presence of heavy metals in these pigments is a deterrent to their commercial use. Such pigments can cause serious health and environmental hazards.[10,11] Synthesis of efficient substitutes for hazardous pigments without compromising the optical characteristics and stability is one of the challenges faced by manufacturers. Environmental friendliness, economic viability and high stability are the main objectives of present-day pigment research.[12–15] Apart from the aesthetic aspects, the functional properties of pigments such as solar reflectance, magnetic nature, corrosion inhibition, *etc.* are also under exploration.[1,16] Earth's temperature has risen by 0.18 °C per decade since 1981.[17] The rising global temperature will lead to a climatic catastrophe if left unaddressed. About 52% of the solar spectrum consist of NIR.[18] These NIR radiations are responsible for the heat build-up from solar radiation. To deal with the heat build-up inside buildings, cooling facilities which consume an immense amount of energy are in use. Here arises the significance of NIR reflecting cool pigment coatings, which has an instantaneous effect as well as a long-term impact on rising global temperature.[19,20] The instant effect is nothing but the cooler interiors provided by the NIR reflecting pigment-coated buildings even in the midst of high solar irradiance. The long-term impact occurs from the energy conserved by the utilization of cool coatings instead of air conditioning and other cooling appliances. In the long run, conservation of the energy spent on cooler interiors can lead to a more sustainable and eco-friendly mode of energy utilization.

We have chosen the less explored $TiZn_2O_4$ inverse spinel system as our parent material for investigation.[21] By incorporating Cu^{2+} and Fe^{3+} ions into the $TiZn_2O_4$ lattice, we have developed a series of pigment compositions with colours ranging from greenish-yellow to reddish-brown. Here we report $TiZn_2O_4$-based pigments as affordable, high NIR reflecting and eco-friendly alternatives to many of the environmentally malignant and high-cost commercial pigments.

Experimental

Materials

Zinc nitrate ($Zn(NO_3)_2{\cdot}6H_2O$, Alfa Aesar, 98%), titanium isopropoxide ($Ti(OCH(CH_3)_2)_4$, Aldrich Chemistry, 97%), cupric

[a] *Department of Chemistry, University of Calicut, Kerala, 673635, India*
[b] *Department of Chemistry, Central University of Kerala, 671316, India*
[c] *Department of Environmental Studies, Kannur University, Kerala, India. E-mail: pperiyat@kannuruniv.ac.in*

† Electronic supplementary information (ESI) available. See DOI: https://doi.org/10.1039/d2ma00537a

nitrate trihydrate ($Cu(NO_3)_2{\cdot}3H_2O$, Alfa Aesar, 98%), ferric nitrate nonahydrate ($Fe(NO_3)_3{\cdot}9H_2O$, Alfa Aesar, 98%) and citric acid monohydrate ($C_6H_8O_7{\cdot}H_2O$, Vetec AR, 99.5%) were used as received. Commercial titanium dioxide (TiO_2) powder and acrylic repair material (DPI RR cold cure) were used for coating application studies.

Synthesis

The pigments of formulated stoichiometries were developed by the solution combustion method. Stoichiometric amounts of metal nitrate precursors were dissolved in a minimum amount of distilled water. Titanium isopropoxide was separately dissolved in 10% HNO_3 solution and added to the former solution of metal nitrates. Then, the calculated amount of citric acid was added as a fuel (the fuel-to-oxidiser ratio was maintained at 0.4). The precursor solution was placed on a hotplate with constant stirring at a temperature of 250 °C. The reactant mixture slowly transformed into a viscous gel which on combustion formed a fluffy voluminous solid. The obtained solids were ground using a mortar and pestle and the finely powdered samples were then transferred to crucibles and placed in a muffle furnace for calcination at a temperature of 800 °C for 3 h to obtain the pigment powders of desired compositions. The structural compositions of the Cu^{2+} and Fe^{3+} doped series of pigments are given in Table 1 along with their abbreviations.

Preparation of coatings and thermal shielding evaluation

Selected pigment compositions were used to make NIR reflecting coatings over concrete and aluminium sheets. The preparation of NIR reflecting coatings was done in two steps. The first step involves the coating of a concrete cement block/Al sheet with TiO_2, which is a highly NIR reflecting pigment. In the next step, the designed pigments are coated onto the TiO_2 precoated concrete/Al sheets. For this, the developed pigments are mixed with acrylic binder in the weight ratio of 1 : 1. The mixture is ultrasonicated thoroughly for 30 minutes to ensure the even dispersion of the pigment particles in the binder. The resultant emulsion was coated onto a TiO_2-coated concrete/Al sheet and was allowed to dry in air. The concrete coatings were then subjected to solar reflectance measurements and chromatic studies using the ASTM standard number G173-03 model and CIE 1976 $L^*a^*b^*$ colour scheme, respectively.

Table 1 Composition and the corresponding abbreviations of the developed $TiZn_2O_4$ based pigments

Composition	Abbreviation
$TiZn_2O_4$	TZ
$TiZn_{1.8}Cu_{0.2}O_4$	TZC-0.2
$TiZn_{1.6}Cu_{0.4}O_4$	TZC-0.4
$TiZn_{1.4}Cu_{0.6}O_4$	TZC-0.6
$TiZn_{1.2}Cu_{0.8}O_4$	TZC-0.8
$TiZn_1Cu_1O_4$	TZC-1
$TiZn_{1.8}Fe_{0.2}O_{4.1}$	TZF-0.2
$TiZn_{1.6}Fe_{0.4}O_{4.2}$	TZF-0.4
$TiZn_{1.4}Fe_{0.6}O_{4.3}$	TZF-0.6
$TiZn_{1.2}Fe_{0.8}O_{4.4}$	TZF-0.8
$TiZn_1Fe_1O_{4.5}$	TZF-1

The thermal shielding effect of the developed pigment compositions was evaluated using an experimental setup. The setup consists of two foam boxes ($8 \times 8 \times 8$ cm^3) with Al sheet roofing of dimensions 10×10 cm^2 coated with the developed pigments as per the procedure mentioned above. A thermocouple was inserted into the foam box just 2 cm below the roof. The foam boxes with pigment-coated roofs were then placed under an IR lamp (Philips, 250 watts), 40 cm below, for 1 hour. The temperatures were recorded at 10 minute intervals.

Characterisation

The X-ray diffraction studies of the developed pigments were carried out using a PANalytical X'Pert3 Powder with Cu-Kα radiation of 1.5405 Å wavelength. The X-ray diffraction data were observed over the 2θ range of 10–90° with a step size of 0.0167 and a time per step of 15.24 s. The lattice parameters of the samples were calculated by the Rietveld refinement method on the PXRD patterns using the GSAS-EXPGUI program.[22] XPS analysis of selected compositions was performed using an XPS spectrometer (Omicron Nanotechnology Ltd.) and all binding energies were referenced to the C 1s peak (284.8 eV) arising from adventitious carbon. Surface morphologies were analysed using a Zeiss Sigma field emission scanning electron microscope. Optical studies were carried out using a Jasco V-770 UV-Visible-NIR spectrometer with an integrating sphere attachment. The NIR measurements were carried out with polytetrafluoroethylene (PTFE) as the reference. The band-gaps of the developed pigment compositions were obtained from the diffuse reflectance spectra using the Kubelka–Munk equation, *i.e.*,

$$F(R) = \frac{1 - R^2}{2R}$$

where R is the observed reflectance of the samples.

The thermal stability of the developed pigments was studied using a PerkinElmer STA 8000 TG-DTA analyser in the temperature range of 30–1000 °C.

The chromatic characteristics were calculated using the CIE 1976 $L^*a^*b^*$ colour scheme of Commission Internationale De l'eclairage (CIE).[21] Here L^* represents the lightness scale which ranges from 0 (black) to 100 (white). The transition from green (−ve) to red (+ve) is represented by the a^* coordinate and b^* gives the blue (−ve) to yellow (+ve) transition. Another factor, c^*, known as chroma represents the saturation of colour and is calculated using the equation:

$$C^* = [(a^*)^2 + (b^*)^2]^{1/2}$$

The hue angle h° is expressed in degrees and it ranges from 0° to 360° and is calculated using the formula:

$$h^\circ = \tan^{-1}(b^*/a^*)$$

Solar reflectance measurements were carried out according to the ASTM standard number G173-03.[23] The solar reflectances of the developed pigments were calculated over the wavelength

range of 700–2500 nm using the equation:

$$R* = \frac{\int_{700}^{2500} r(\lambda) i(\lambda) d(\lambda)}{\int_{700}^{2500} i(\lambda) d(\lambda)}$$

where $r(\lambda)$ is the spectral reflectance of the sample obtained experimentally and $i(\lambda)$ is the standard solar spectral irradiance (W m^{-2} mm^{-1}) according to the ASTM standard model G173-03.

Results and discussion

X-ray diffraction studies

The XRD pattern of TZ, *i.e.* the undoped version of $TiZn_2O_4$, along with the reference pattern is shown in Fig. 1. The PXRD pattern of TZ can be indexed to the cubic crystal structure belonging to the $Fd\bar{3}m$ space group (JCPDS00-025-1164).[21] $TiZn_2O_4$ has an inverse spinel structure in which half of the Zn^{2+} ions occupy the tetrahedral voids and the other half occupy octahedral voids along with Ti^{4+} ions in the lattice.[24]

The XRD patterns of the synthesized Cu doped $TiZn_2O_4$ compositions having the general formula $TiZn_{2-x}Cu_xO_4$ (where x ranges from 0 to 1) are shown in Fig. 2. Upon examination, Cu^{2+} doped variants, *i.e.* TZC-0.2, TZC-0.4, TZC-0.6, TZC-0.8 and TZC-1, were also found to have a cubic crystal structure with the $Fd\bar{3}m$ space group. In addition to the cubic $TiZn_2O_4$ phase, the XRD patterns of TZC-0.2 and TZC-0.4 exhibited ZnO, that of TZC-0.6 showed TiO_2 and those of TZC-0.8 and TZC-1 contained the CuO phase in negligible amounts. Since $TiZn_2O_4$ had an inverse spinel structure, upon Cu^{2+} doping the Zn^{2+} ions present in the octahedral sites of the inverse spinel lattice were replaced by Cu^{2+} ions. The crystal field stabilization energy of Cu^{2+} plays a crucial role here.[25,26] Even after doping of Cu^{2+} ions into the $TiZn_2O_4$ lattice, the XRD patterns showed no significant phase changes or additional peaks, except the minute ZnO, TiO_2 and CuO peaks. Upon close examination, the XRD patterns of Cu^{2+} doped variants showed a narrow shift towards higher 2θ values. This can be attributed to the slightly smaller ionic radii of Cu^{2+} (73 pm) compared to Zn^{2+} (74 pm) ions.

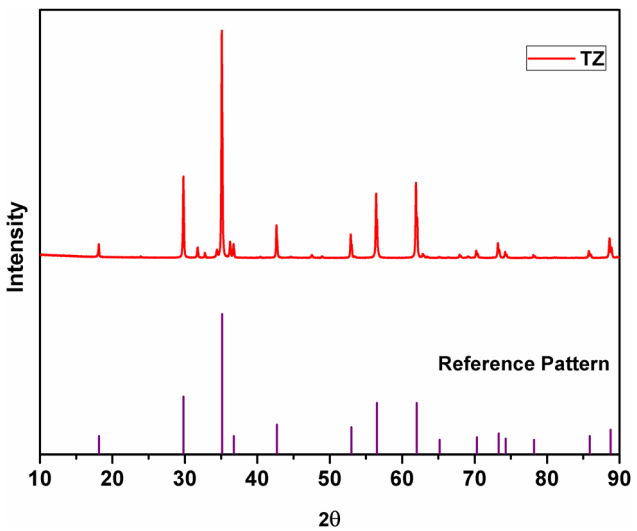

Fig. 1 XRD pattern of $TiZn_2O_4$ and the reference pattern.

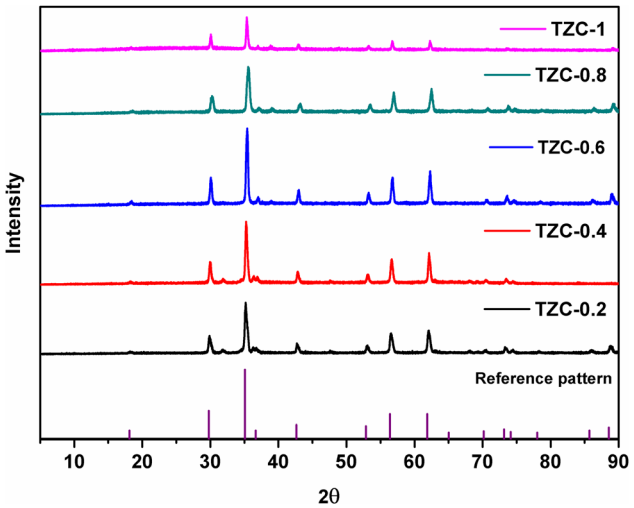

Fig. 2 X-ray diffraction patterns of the synthesized Cu^{2+} doped $TiZn_2O_4$ compositions.

To understand the TZ crystal structure and the changes occurring in the lattice upon doping with Cu^{2+} ions, we have carried out Rietveld refinement studies of the synthesized samples. Fig. 3 shows the crystal structures drawn from the lattice parameters obtained by the Rietveld refinement of TZ and TZC-0.4. The experimental and refined patterns obtained after the Rietveld refinement of TZ and two of the best promising candidates for NIR reflecting pigment applications, *i.e.* TZC-0.2 and TZC-0.4, are shown in Fig. 4. The lattice parameters obtained for TZ and Cu^{2+} doped $TiZn_2O_4$ compositions after Rietveld refinement are shown in Table 2. Rietveld refinement was performed on all the samples using the structural parameter of cubic $TiZn_2O_4$. Refinement of the XRD patterns with these parameters proceeded smoothly and the refinement details of the rest of the Cu^{2+} doped $TiZn_2O_4$ compositions are given in the ESI† (Fig. S1 and Table S1).[21] Table 2 shows a reduction in lattice parameters and cell volume with an increase in Cu^{2+} doping. The decrease in lattice parameters and cell volume can be attributed to the smaller ionic radii of Cu^{2+} relative to Zn^{2+}. The refinement data obtained show that the doping of Cu^{2+} into $TiZn_2O_4$ proceeded as

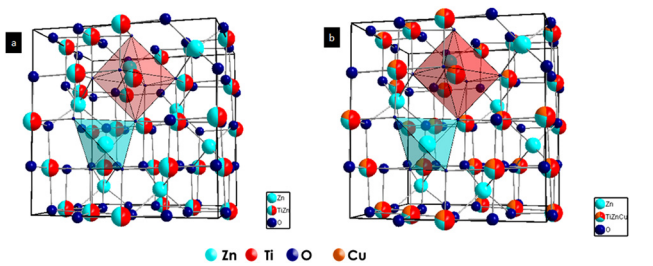

Fig. 3 Crystal structures of (a) TZ and (b) TZC-0.4 obtained through Rietveld refinement studies.

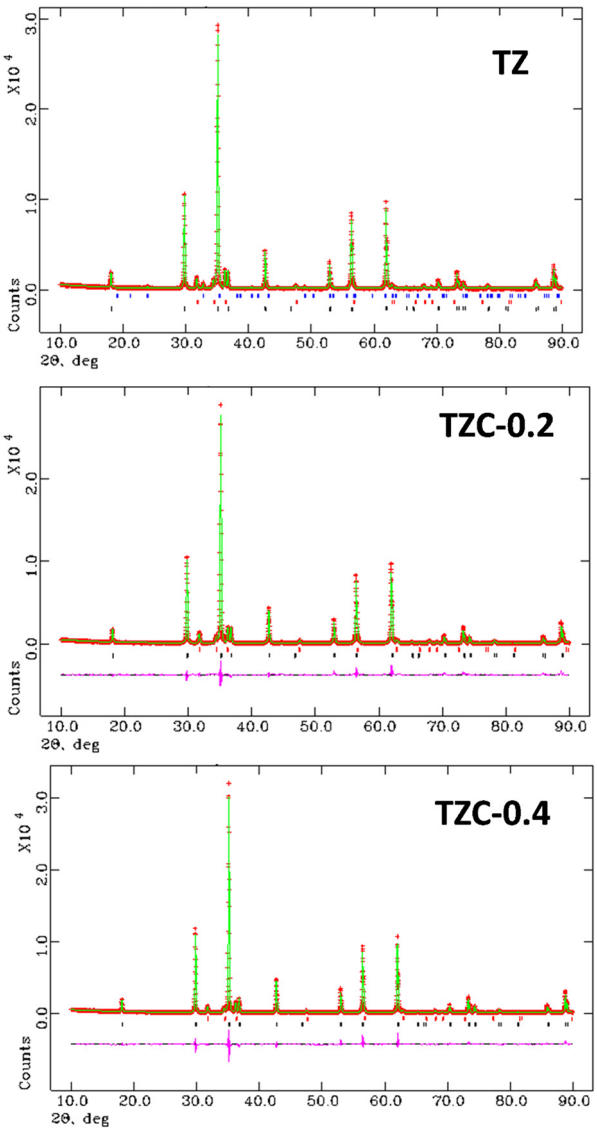

Fig. 4 The experimental and refined patterns obtained on Rietveld analysis of TZ, TZC-0.2 and TZC-0.4 samples.

Table 2 The reliability factors and lattice parameters obtained for TZ and the $TiZn_{2-x}Cu_xO_4$ series by Rietveld refinement studies

Samples	χ^2	wR_p (%)	R_p (%)	a (Å)	Volume
TZ	3.75	9.55	7.40	8.4650(0)	606.6
TZC-0.2	3.65	9.37	7.24	8.4596(0)	605.4
TZC-0.4	4.24	10.44	8.14	8.4542(0)	604.3
TZC-0.6	5.32	8.51	11.44	8.4510(0)	603.6
TZC-0.8	3.79	9.64	7.22	8.4493(5)	603.2
TZC-1	4.81	10.90	8.18	8.4367(0)	600.5

planned. The fractional coordinates, sites occupied and extent of occupancy of each atom upon completion of Rietveld refinement of pristine and two best promising Cu^{2+} doped $TiZn_2O_4$ compositions, *i.e.*, TZC-0.2 and TZC-0.4, are shown in Table 3. The observed XRD patterns are in good agreement with the calculated Cu^{2+} doped $TiZn_2O_4$ models. The extent of

Table 3 The fractional coordinates, sites occupied and extent of occupancy obtained upon Rietveld refinement for TZ, TZC-0.2 and TZC-0.4 compositions

Atom	Site	x	y	z	U_{iso}	Occupancy
TZ						
Zn(1)	8a	0.125	0.125	0.125	0.01745	1
Ti	16d	0.5	0.5	0.5	0.00953	0.5
Zn(2)	16d	0.5	0.5	0.5	0.01975	0.5
O	32e	0.25885	0.25885	0.25885	0.01897	1
TZC-0.2						
Zn(1)	8a	0.125	0.125	0.125	0.01831	1
Ti	16d	0.5	0.5	0.5	0.00848	0.5
Zn(2)	16d	0.5	0.5	0.5	0.01802	0.4
Cu	16d	0.5	0.5	0.5	0.00908	0.1
O	32e	0.25918	0.25918	0.25918	0.01937	1
TZC-0.4						
Zn(1)	8a	0.125	0.125	0.125	0.01849	1
Ti	16d	0.5	0.5	0.5	0.00748	0.5
Zn(2)	16d	0.5	0.5	0.5	0.01528	0.3
Cu	16d	0.5	0.5	0.5	0.01698	0.2
O	32e	0.25895	0.25895	0.25895	0.02028	1

agreement is evident from the χ^2, R_p and wR_p values obtained upon refinement. The reduction in lattice volume and cell edge lengths due to the incorporation of Cu^{2+} ions is evident from the refinement data.

The Fe^{3+} doped $TiZn_2O_4$ compositions having the general formula $TiZn_{2-x}Fe_xO_{4+\delta}$ (where x = 0.2, 0.4, 0.6, 0.8, 1 and $\delta = x/2$) showed XRD patterns identical to that of the cubic structure of $TiZn_2O_4$. The XRD patterns of the $TiZn_{2-x}Fe_xO_{4+\delta}$ series are shown in Fig. 5.

From the XRD data, it is evident that the Fe^{3+} doped $TiZn_2O_4$ structures belong to the $Fd\bar{3}m$ space group. The proposed crystal structure for the $TiZn_{2-x}Fe_xO_{4+\delta}$ composition involves an inverse spinel structure in which Fe^{3+} ions are expected to occupy the octahedral sites and site allocation is given by the formula $Ti_{(oh)}Zn_{1(Td)}Zn_{1-x(oh)}Fe_{x(Oh)}O_{4+\delta}$. The allocation of Fe^{3+}

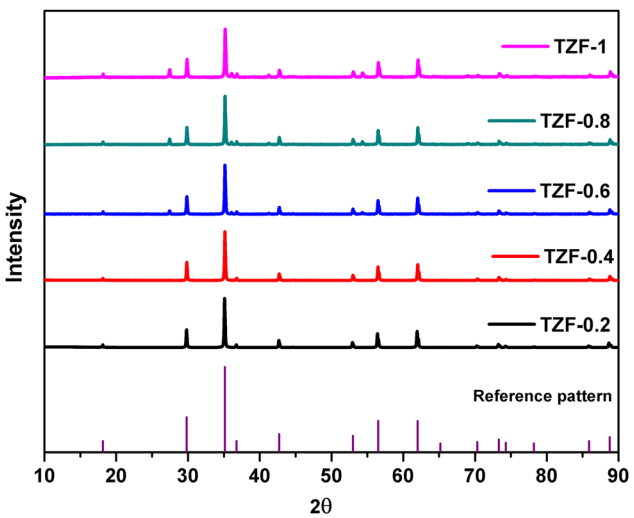

Fig. 5 X-ray diffraction patterns of the synthesized Fe^{3+} doped $TiZn_2O_4$ compositions.

into the octahedral sites is confirmed with the help of Rietveld refinement and XPS in a later section. The doping of Fe^{3+} into the octahedral Zn^{2+} positions was manifested as a shift in the XRD peaks towards higher 2θ values. This is mainly due to the smaller ionic radii of Fe^{3+} compared to Zn^{2+}. The replacement of octahedral Zn^{2+} ions by Fe^{3+} may result in a reduction of lattice distances.

The effect of Fe^{3+} doping on the $TiZn_2O_4$ crystal structure was evaluated with the help of Rietveld refinement. Similar to the Cu^{2+} doped $TiZn_2O_4$ compositions, the cubic structure was taken as the starting model for refinement. The refined crystal structure for TZF-0.4 is shown in Fig. 6. The experimental and refined patterns for TZF-0.2 and TZF-0.4 are shown in Fig. 7. The lattice parameters for TZ and $TiZn_{2-x}Fe_xO_{4+\delta}$ are listed in Table 4 along with refinement reliability factors. In addition, refinement parameters along with atom positions and site occupancies of TZF-0.2 and TZF-0.4 are provided in Table 5. The refinement details of the remaining compositions are presented in Fig. S2 and Table S2 (ESI†). The lattice distances obtained by refinement studies show a gradual decrease with an increase in Fe^{3+} ion doping into the lattice. The smaller ionic radii of Fe^{3+} compared to Zn^{2+} ions are responsible for this reduction.

To confirm the successful doping of Fe^{3+} ions into the octahedral sites, we have carried out XRD refinement studies using three different starting models. The first model has the general formula $Ti_{(oh)}Zn_{1(Td)}Zn_{1-x(oh)}Fe_{x(Oh)}O_{4+\delta}$ where the Fe^{3+} ions are completely allotted to the octahedral sites. The second one $Ti_{(oh)}Zn_{1(Oh)}Zn_{1-x(Td)}Fe_{x(Td)}O_{4+\delta}$ has got all the Fe^{3+} ions occupying the tetrahedral voids. The third model assumes an equal distribution of Fe^{3+} ions between octahedral and tetrahedral voids, *i.e.*, $Ti_{(oh)}Zn_{1-x/2(Oh)}Fe_{x/2(Oh)}Zn_{1-x/2(Td)}Fe_{x/2(Td)}O_{4+\delta}$. After the completion of refinement using all the three models, a comparison of the chi square, R_p and wR_p values given in Table 6 revealed that the general composition of Fe^{3+} doped $TiZn_2O_4$ samples is $Ti_{(oh)}Zn_{1(Td)}Zn_{1-x(Oh)}Fe_{x(Oh)}O_{4+\delta}$.

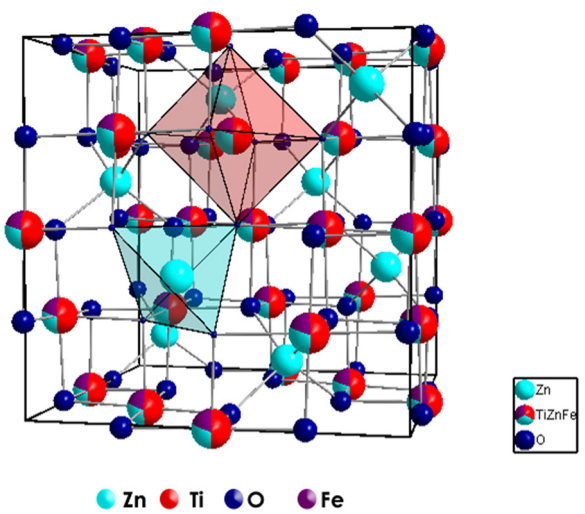

Fig. 6 Crystal structures of TZF-0.4 obtained through Rietveld refinement studies.

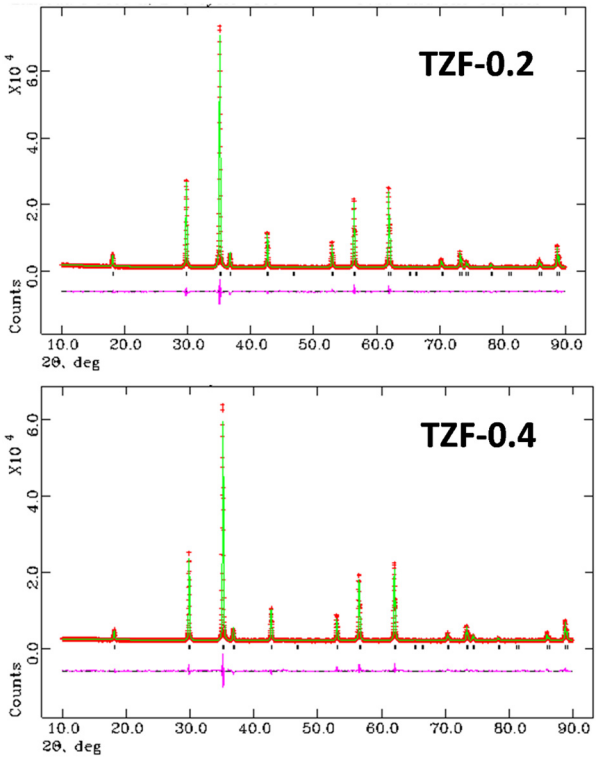

Fig. 7 The experimental and refined patterns obtained on Rietveld analysis of TZF-0.2 and TZF-0.4 samples.

Table 4 The reliability factors and lattice parameters obtained for TZ and the $TiZn_{2-x}Fe_xO_4$ series by Rietveld refinement studies

Samples	χ^2	wR_p (%)	R_p (%)	a (Å)	Volume
TZ	3.75	9.55	7.40	8.4650(0)	606.6
TZF-0.2	3.82	4.48	3.28	8.4615(0)	605.8
TZF-0.4	3.81	3.79	2.66	8.4511(0)	603.6
TZF-06	1.71	3.74	2.79	8.4491(0)	603.2
TZF-0.8	1.89	3.59	2.59	8.4497(0)	603.3
TZF-1	1.29	2.80	2.15	8.4493(0)	603.2

Table 5 The fractional coordinates, sites occupied and extent of occupancy obtained upon Rietveld refinement for TZF-0.2 and TZF-0.4 compositions

Atom	Site	x	y	z	U_{iso}	Occupancy
TZF-0.2						
Zn(1)	8a	0.125	0.125	0.125	0.01240	1
Ti	16d	0.5	0.5	0.5	0.00471	0.5
Zn(2)	16d	0.5	0.5	0.5	0.01612	0.4
Fe	16d	0.5	0.5	0.5	0.00134	0.1
O	32e	0.25840	0.25840	0.25840	0.01363	1
TZF-0.4						
Zn(1)	8a	0.125	0.125	0.125	0.01668	1
Ti	16d	0.5	0.5	0.5	0.01017	0.5
Zn(2)	16d	0.5	0.5	0.5	0.01630	0.3
Fe	16d	0.5	0.5	0.5	0.00654	0.2
O	32e	0.25868	0.25868	0.25868	0.01833	1

The refinement details of models 2 and 3 are shown in Fig. S3 and Table S3 (ESI†). Thus, it is evident that both Cu^{2+}

Table 6 The reliability factors and lattice parameters obtained for three different models of site allocation in $TiZn_{2-x}Fe_xO_4$ by Rietveld refinement studies

	χ^2	wR_p (%)	R_p (%)	a (Å)	Volume
Model 1	3.82	4.48	3.28	8.4615(0)	605.8
Model 2	6.121	5.67	4	8.4604(2)	605.6
Model 3	6.522	5.85	4.06	8.4575(2)	604.9

and Fe^{3+} ions occupy the octahedral sites in the inverse spinel lattice of $TiZn_2O_4$. The percentages of main and secondary phases calculated from Rietveld refinement for each of the developed compositions are given in Table S4 (ESI†).

XPS analysis

The XPS measurements were carried out mainly to confirm the oxidation state and site of occupancy of Fe in $TiZn_{2-x}Fe_xO_{4+\delta}$ compositions. Cu^{2+} had CFSE considerations towards the octahedral sites, which was further confirmed by Rietveld refinement studies.[26] So the TZC series does not require any additional assurance on its Cu^{2+} site of occupancy. Such a conclusion cannot be made in the case of Fe^{3+} doped samples without XPS measurements. Here we have performed the XPS analysis of TZF-0.2 as a model system. The XPS spectra of TZF-0.2 in the regions of O, Ti, Zn and Fe are shown in Fig. 8. The O 1s signal of TZF-0.2 shown in Fig. 8a can be deconvoluted into three peaks with binding energies centred at 529.7, 531.6 and 532.8 eV which correspond to lattice oxygen, oxygen-deficient regions and surface hydroxyl groups, respectively.[27] In the case of Zn^{2+}, the peaks corresponding to Zn $2p_{3/2}$ and Zn $2p_{1/2}$ states were observed at binding energies of 1021 and 1044 eV (ESI,† Fig. S4).[28] To confirm the distribution of Zn^{2+} among the octahedral and tetrahedral sites, we have carried out the deconvolution of the Zn $2p_{3/2}$ peak. From the literature, it is evident that the $2p_{3/2}$ signal that appears at 1019 eV corresponds to Zn^{2+} ions occupying tetrahedral sites and the signal around 1021 eV corresponds to octahedral sites occupying Zn^{2+} ions.[29] Here we have deconvoluted the Zn $2p_{3/2}$ signal into two peaks corresponding to Zn^{2+} ions occupying octahedral and tetrahedral sites as shown in Fig. 8b. In the case of Ti, Ti^{4+} shows a single peak centred at 458.3 which belongs to the Ti $2p_{3/2}$ state of octahedral coordination as shown in Fig. 8c.[27] Also, the Fe $2p_{3/2}$ peak of TZF-0.2 is observed at 709.8 eV and the Fe $2p_{1/2}$ peak is observed at 723.3 eV.[27] The presence of a satellite peak at 718.6 eV confirmed the oxidation state of Fe as 3+.[30,31] Apart from this, due to spin–orbit and electrostatic interactions present in high spin early transition metal ions, each of the Fe $2p_{3/2}$ and $2p_{1/2}$ peaks can be deconvoluted into four peaks as shown in Fig. 8d.[32,33] The fitting of Fe 2p XPS spectrum into four multiplets further ensured the presence of

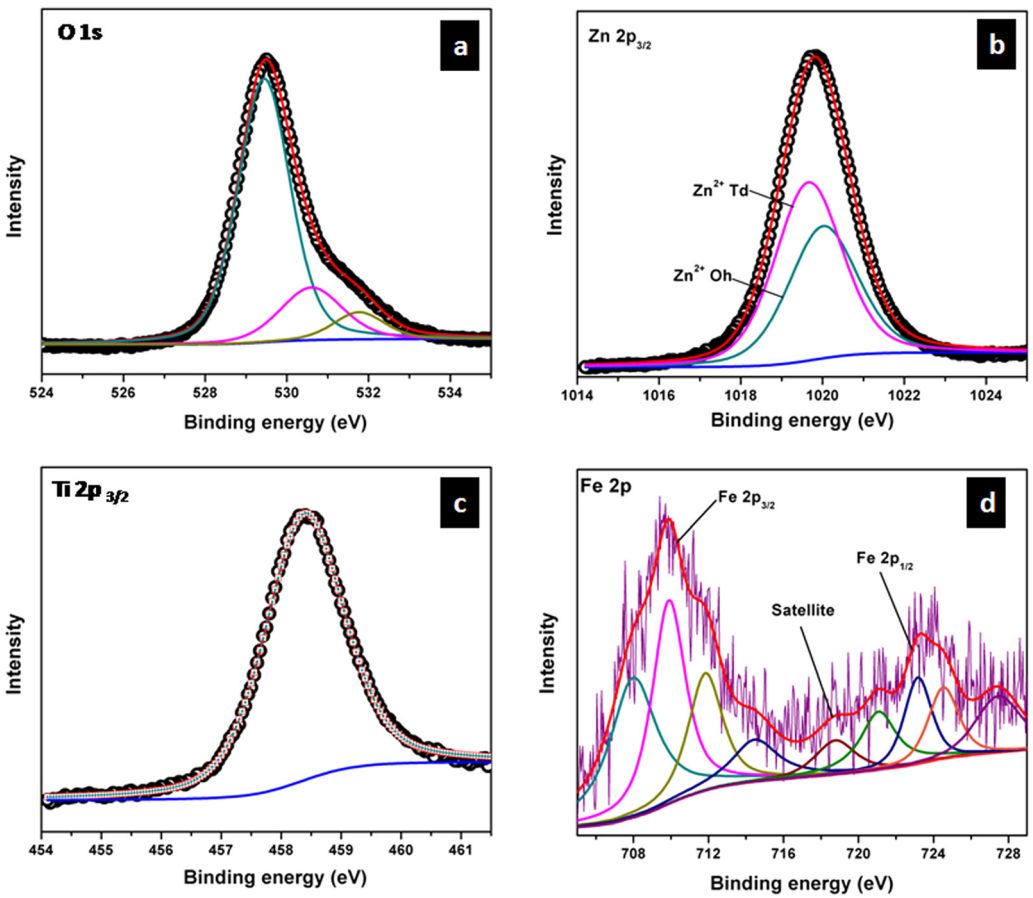

Fig. 8 High-resolution XPS spectra of (a) O 1s, (b) Zn $2p_{3/2}$, (c) Ti $2p_{3/2}$ and (d) Fe 2p core levels in TZF-0.2.

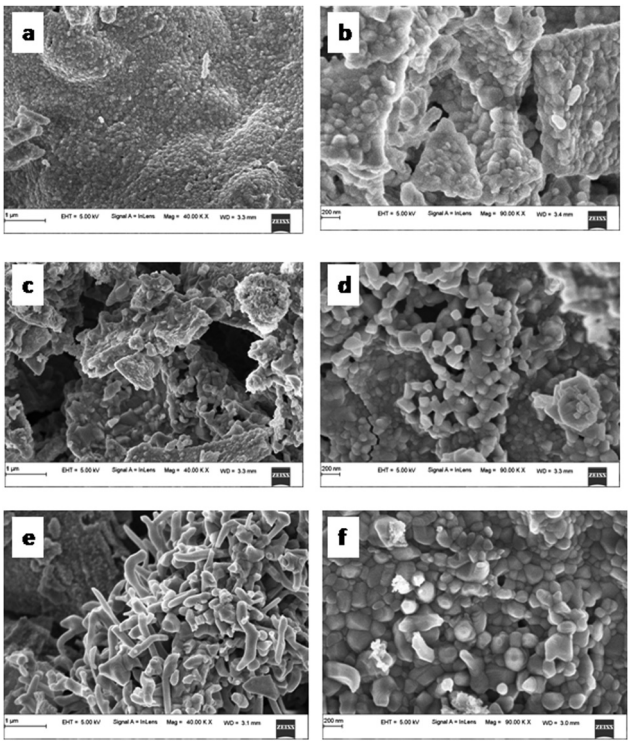

Fig. 9 FE-SEM images of (a and b) TZ, (c and d) TZC-0.2 and (e and f) TZC-0.4 samples.

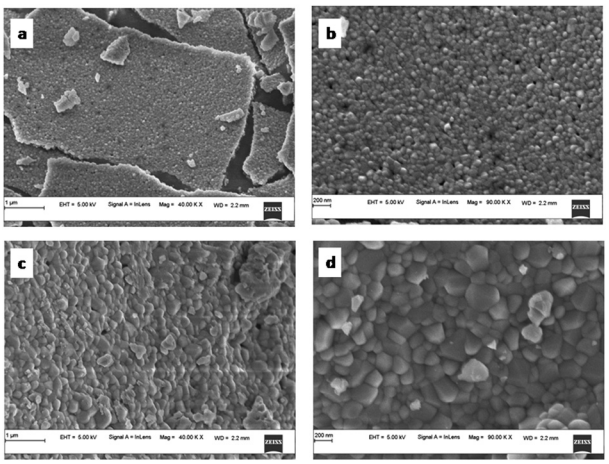

Fig. 10 FE-SEM images of (a and b) TZF-0.2 and (c and d) TZF-0.4 samples.

Fe^{3+} ions in octahedral sites.[33,34] Thus, the XPS measurement results are found to be in exact agreement with Rietveld refinement data and expected stoichiometries.

FE-SEM

The SEM micrographs of TZ, TZC-0.2 and TZC-0.4 are shown in Fig. 9. The SEM images show extended aggregation of particles and the aggregates are found to be in the micrometre regime. With Cu^{2+} doping, there is a variation in the shape of the aggregates. The particles are getting transformed from the spherical form into needle-like structures with an increase in the Cu^{2+} dopant amount. Fig. 10 shows that, in the case of TZF-0.2 and TZF-0.4, the extent of aggregation is somewhat similar to that found in TZ. From Fig. 10, TZF-0.2 is found to contain flake-like aggregates which are smaller than those of TZF-0.4. The increment in the size of the aggregates results in a reduction in NIR reflectance.[35]

UV-visible diffuse reflectance studies

The UV-visible diffuse reflectance spectra of Cu^{2+} doped $TiZn_2O_4$ pigment powders are shown in Fig. 11a. Here we can see that the undoped $TiZn_2O_4$, *i.e.* TZ, shows no characteristic absorption in the visible region and, as a result, it appears white. With the incorporation of Cu^{2+} ions into the $TiZn_2O_4$ lattice, a gradual shift of the absorption edges towards higher wavelengths is seen. This bathochromic shift can be explained by the bandgap measurements made using the Kubelka–Munk function. The bandgaps of all the developed Cu^{2+} doped $TiZn_2O_4$ compositions are shown in Table 4. From Fig. 11b, the gradual decrease in bandgaps which is responsible for the bathochromic shift is evident. All the Cu^{2+} doped variants exhibited absorptions in the visible region. The absorption in the region of 740–800 nm can be attributed to the ^2E_g–$^2T_{2g}$ transition in a d^9 octahedral system.[36] One such absorption centred around 800 nm helps in imparting a green tint to TZC-0.2. At the same time, for TZC-0.4, the absorption is around 780 nm which accounts for its yellow colour. Upon increasing the Cu^{2+} ion concentration, the absorption band gets broader and extends all over the visible region. Thus, the compositions become darker on increasing the Cu^{2+} concentration.

In the case of Fe^{3+} doped $TiZn_2O_4$ pigment powders, the observed changes in the diffuse reflectance spectra are shown in Fig. 12a. TZ which displays no significant absorption in the visible region gradually shows absorptions within the range of 350 to 900 nm with the introduction of Fe^{3+} into the $TiZn_2O_4$ structure. The changes in the optical properties of TZF-0.2, TZF-0.4, TZF-0.6, TZF-0.8 and TZF-1 are due to the incorporation of Fe^{3+} into the octahedral sites of the $TiZn_2O_4$ lattice as confirmed by the XRD refinement studies. Among the absorptions shown by Fe^{3+} doped $TiZn_2O_4$, the one around 380 nm can be attributed to the $^6A_1(^6S) \rightarrow {}^4E(^4D)$ transition.[36] Again the absorptions around 430 and 470 nm are due to the $^6A_1(^6S) \rightarrow {}^4E(^4G)$ and $^6A_1(^6S) \rightarrow {}^4A_1(^4G)$ transitions. The Fe^{3+} doped samples show a significant reduction in reflectance around 650 and 800 nm, which results from $^6A_1(^6S) \rightarrow {}^4T_2(^4G)$ and $^6A_1(^6S) \rightarrow {}^4T_1(^4G)$ bands.[36,37] With an increase in Fe^{3+} dopant concentration, the $^6A_1(^6S) \rightarrow {}^4T_2(^4G)$ and $^6A_1(^6S) \rightarrow {}^4T_1(^4G)$ bands become more superior and the absorption becomes broader and extends over the range of 500–900 nm. The extension of the absorption edges towards higher wavelengths due to the gradual decrease in bandgap with an increase in dopant Fe^{3+} ion concentration is shown in Fig. 12b. The calculated bandgap values are given in Table 5. Here we can see that TZF-0.2 shows light yellowish-orange colour which gradually transforms into orange and brownish-orange as we move along the series. The yellowish-orange colour in TZF-0.2 arises

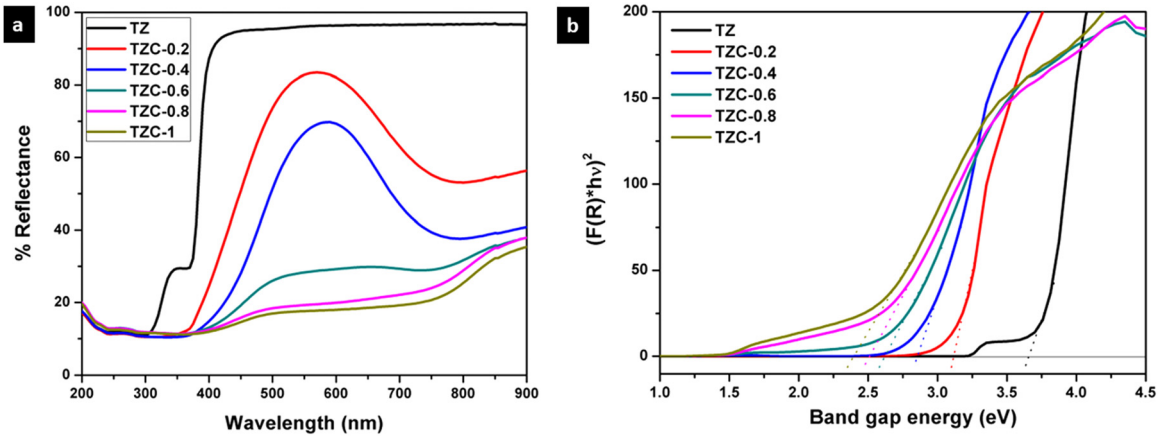

Fig. 11 (a) UV-visible diffuse reflectance spectra and (b) Kubelka–Munk plots of Cu^{2+} doped $TiZn_2O_4$ pigments.

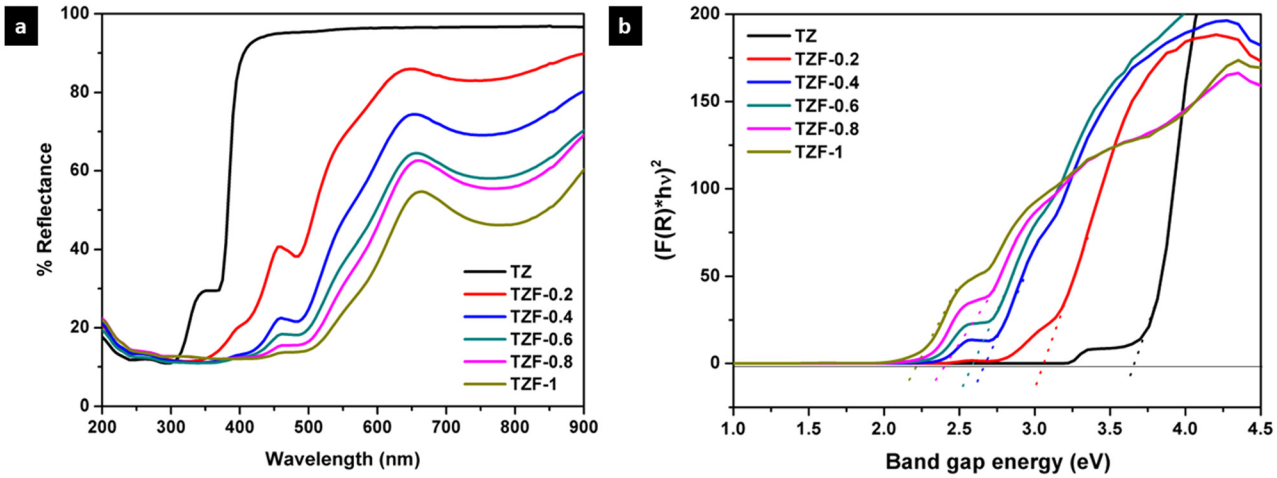

Fig. 12 (a) UV-visible diffuse reflectance spectra and (b) Kubelka–Munk plots of Fe^{3+} doped $TiZn_2O_4$ pigments.

due to the absorption of visible light in the violet-indigo region and TZF-0.2 appears in the complementary yellowish-orange colour. In the case of TZF-0.4, the absorption extends towards the violet-blue region and a corresponding increase in orange hue is observed. As we move from TZF-0.4 to TZF-1, *i.e.* with an increasing concentration of Fe^{3+} ions in $TiZn_2O_4$, the absorptions are found to be in the blue-green region. The extension of visible light absorption towards the green region manifests as an increase in the orange colour intensity.

Near-infrared reflectance analysis

The NIR reflectance in the range of 700–2500 nm, for the Cu^{2+} doped $TiZn_2O_4$ samples, is shown in Fig. 13 along with the solar reflectance spectra of TZ, TZC-0.2 and TZC-0.4. Pure $TiZn_2O_4$ (TZ) shows a solar reflectance of 96.76% in the NIR region. Compared to TZ, the NIR reflection is less for Cu^{2+} doped $TiZn_2O_4$ compositions. Percentage NIR reflectance decreases with an increase in the amount of Cu^{2+} ions. Even though there is a reduction in reflectance along with the Cu^{2+} doped series, TZC-0.2 and TZC-0.4 exhibited attractive colours along with considerable solar reflectance values. The NIR reflectance R^* values for the developed Cu^{2+} incorporated $TiZn_2O_4$ pigment samples along with $BiPO_4$, an already reported yellow pigment, are given in Table 7.[38]

The NIR reflectance of Fe^{3+} doped $TiZn_2O_4$ samples was also determined. The NIR reflectance spectra of the Fe^{3+} incorporated pigment series are shown in Fig. 14. The percentage of NIR reflectance R^* values for Fe^{3+} doped $TiZn_2O_4$ pigments and commercial $BiVO_4$ are given in Table 8. Both TZF-0.2 and TZF-0.4 exhibited percentage NIR reflectance values higher than $BiVO_4$.[39] Compared to the percentage reflectance of TZ, there is a reduction of reflectance around the 700–1600 nm region, with the substitution of Zn^{2+} ions in octahedral sites with Fe^{3+} ions. The introduction of chromophore Fe^{3+} ions into the $TiZn_2O_4$ lattice enhances the visual appearance by imparting different shades of orange colour to the samples. The observed colours ranged from yellowish-orange to reddish-brown. Despite having a reduction in solar reflectance across the Fe^{3+} doped series, TZF-0.2 and TZF-0.4 show promising solar reflectance values of 87.81 and 77.83%, respectively.

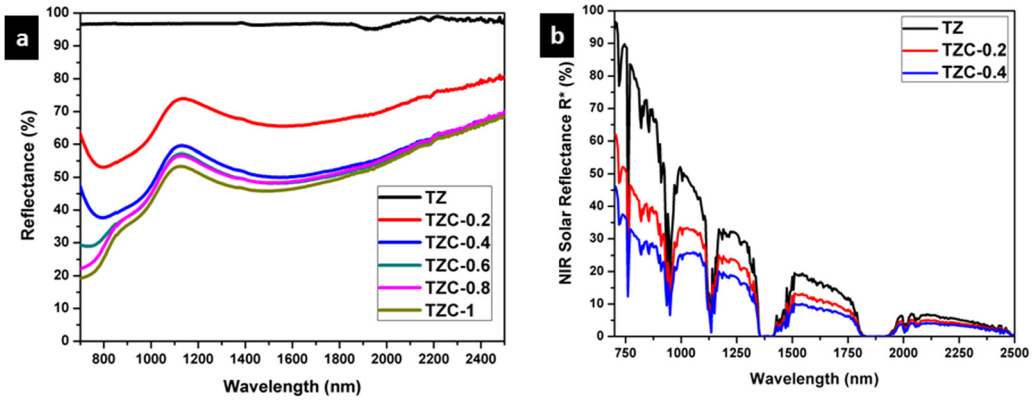

Fig. 13 (a) NIR reflectance spectra of Cu^{2+} doped $TiZn_2O_4$ pigment powders and (b) solar reflectance spectra of TZ, TZC-0.2 and TZC-0.4 samples.

Table 7 Bandgap, percentage NIR reflectance and CIE $L^*a^*b^*$ parameters of pure and Cu^{2+} doped $TiZn_2O_4$ compositions

	Bandgap (eV)	NIR reflectance (R^*) (%)	L^*	a^*	b^*	c	h°
TZ	3.54	96.76	98.41	−0.05	0.99	0.99	92.89
TZC-0.2	3.12	62.83	91.12	−7.50	24.18	25.32	107.23
TZC-0.4	2.93	47.61	82.92	−5.48	36.41	36.82	98.56
TZC-0.6	2.65	43.19	59.61	−2.44	14.13	14.34	99.79
TZC-0.8	2.51	41.90	50.88	−0.66	7.04	7.07	95.36
TZC-1	2.39	39.13	48.84	−1.08	6.28	6.37	99.76
$BiPO_4$[a]	3.657	86.40	96.85	−0.27	0.64	0.69	112.87

[a] Literature reported.

Chromatic studies

As a part of analysing the chromatic characteristics of the developed pigments, the CIELAB colour coordinates were measured. Fig. 15 shows the photograph of the developed $TiZn_2O_4$ based pigment powders. The CIE $L^*a^*b^*$ parameters of TZ and Cu^{2+} doped compositions along with $BiPO_4$ are listed in Table 7. With the incorporation of Cu^{2+} chromophores, there is a decrease in the lightness coordinate, L^*. At the same time, there is an initial reduction in the a^* value due to the green tint attributed to the Cu^{2+} doping in TZC-0.2, which becomes less negative with a further increase in the Cu^{2+} dopant amount. The increase in yellowish hue from TZ to TZC-0.4 is evident from the rise in b^* values. The b^* values start decreasing from TZC-0.6 onwards. The lightness coordinate L^* also shows a reduction in values, with an increase in Cu^{2+} chromophore concentration. Even though inferior to $BiPO_4$ in NIR reflectance, TZC-0.2 and TZC-0.4 exhibited superior yellow hues compared to $BiPO_4$.[38]

The CIELAB coordinates for Fe^{3+} doped compositions are given in Table 8 along with commercial $BiVO_4$. Here also a reduction in the lightness coordinate with an increase in Fe^{3+} content was observed. Again, as the dopant Fe^{3+} concentration increases, the orange tint was found to be increasing which manifests as an increment in a^* and b^* coordinates. The TZF series exhibited an enhanced red hue represented by the rise in the a^* coordinate with an increase in Fe^{3+} doping. The b^* values clearly show that the yellow hue increases from TZ to TZF-0.4 and then starts diminishing. Fe^{3+}-doped variants managed to retain attractive orange to brownish-orange shades even with increased dopant concentrations. TZF-0.2 and TZF-0.4 managed to exhibit considerable yellow hues even without the use of hazardous elements. Even though commercial $BiVO_4$ exhibited

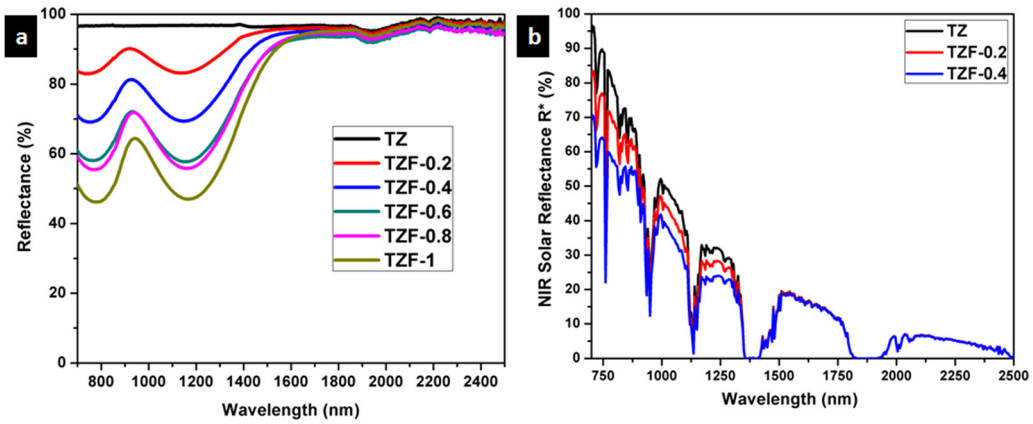

Fig. 14 (a) NIR reflectance spectra of Fe^{3+} doped $TiZn_2O_4$ pigment powders and (b) solar reflectance spectra of TZ, TZF-0.2 and TZF-0.4 samples.

Table 8 Bandgap, percentage NIR reflectance and CIE $L^*a^*b^*$ parameters of pure and Fe^{3+} doped $TiZn_2O_4$ compositions

	Bandgap (eV)	NIR reflectance (R^*) (%)	L^*	a^*	b^*	c	h°
TZ	3.54	96.76	98.41	−0.05	0.99	0.99	92.89
TZF-0.2	3.07	87.81	84.81	6.92	31.72	32.47	77.693
TZF-0.4	2.69	77.83	73.70	14.49	37.78	40.46	69.016
TZF-0.6	2.57	68.73	66.97	16.39	32.84	36.70	63.47
TZF-0.8	2.29	67.44	63.27	19.55	31.54	37.11	58.207
TZF-1	2.19	60.43	57.68	19.70	25.29	32.06	52.081
$BiVO_4$[a]	2.40	73.51	82.43	4.25	76.26	76.38	86.81

[a] Literature reported.

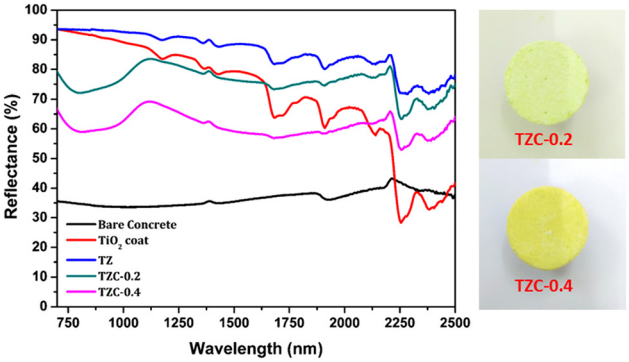

Fig. 16 NIR reflectance spectra of coated TZ, TZC-0.2 and TZC-0.4 in comparison with TiO_2 and bare concrete coatings.

superior yellow colour, TZF-0.2 and TZF-0.4 compositions have higher NIR reflectance and more economic viability.[39]

Coating studies

The NIR reflectance values were calculated for the selected pigment coatings over concrete and Al sheet substrates. Fig. 16 shows the NIR reflectance spectra of TZ, TZC-0.2 and TZC-0.4 coatings over concrete in comparison with bare concrete and TiO_2 coating. Fig. 17 shows the NIR reflectance spectra of TZ, TZF-0.2 and TZF-0.4 pigment coatings on concrete along with bare concrete and TiO_2 coatings. The NIR reflectance R^* values calculated according to the ASTM model for the selected pigment coatings are listed in Table 9 along with their CIE $L^*a^*b^*$ coordinates. Fig. 18 shows the NIR reflectance spectra of TZ, TZC-0.2 and TZC-0.4 coatings over the Al sheet in comparison with the bare Al sheet and TiO_2 coating. Fig. 19 shows the NIR reflectance spectra of TZ, TZF-0.2 and TZF-0.4 pigment coatings on the Al sheet. The NIR reflectance R^* values calculated according to the ASTM model for the selected pigment coatings over the Al sheet are listed in Table 10 along with their CIE $L^*a^*b^*$ coordinates.

Thermal shielding studies

The thermal shielding performance of two best pigment compositions, *i.e.*, TZC-0.2 and TZF-0.2, was evaluated. As described in the experimental section, foam boxes roofed with coated and uncoated Al sheets were placed under an IR lamp (40 cm above the roof) and separate temperature sensors were inserted into the foam boxes to monitor the interior temperature. To evaluate the thermal shielding performance, time-dependent temperature measurements were made for 1 hour. We have carried out the thermal shielding analysis for TZC-0.2 and TZF-0.2 separately and compared the results with those of uncoated Al sheet roofing. The time-dependent temperature measurements made for TZC-0.2 and TZF-0.2 coated roofs along with bare Al sheets are shown in Fig. 20. The time–temperature plots indicate a steady increase in temperature with time initially and then gradually get stabilized over 1 hour. Fig. 21a and b show the difference in interior temperatures observed after 1 hour of IR irradiation for the TZC-0.2 and TZF-0.2 coated and uncoated Al roofing. The TZC-0.2 coating provided an interior 3.6 °C cooler than the uncoated roofing interior. In the case of TZF-0.2, the observed temperature difference was 4.8 °C. Thus, the overall results suggest that TZC-0.2 and TZF-0.2 are promising cool pigment candidates with good NIR reflectance characteristics.

Thermal stability studies

The thermal stability of the developed pigments was studied using thermogravimetric analysis. The thermogravimetric analysis of TZ, TZC-0.2, TZC-0.4, TZF-0.2 and TZF-0.4 was carried out in the presence of air in the temperature range of 30–1000 °C. The TGA and DTA results in Fig. 22 show that the developed pigment compositions exhibit high thermal stability, even above 900 °C. There is no significant weight loss observed or no phase changes in the temperature range of 30–1000 °C. High thermal stability is an essential requirement

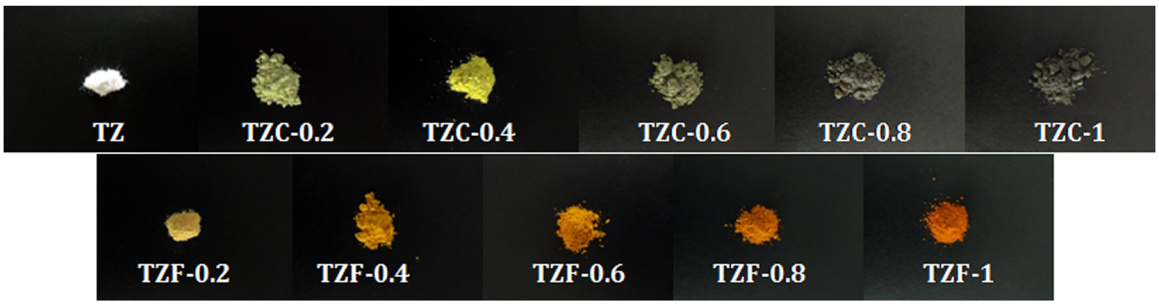

Fig. 15 Photographs of the developed $TiZn_2O_4$ based pigment powders.

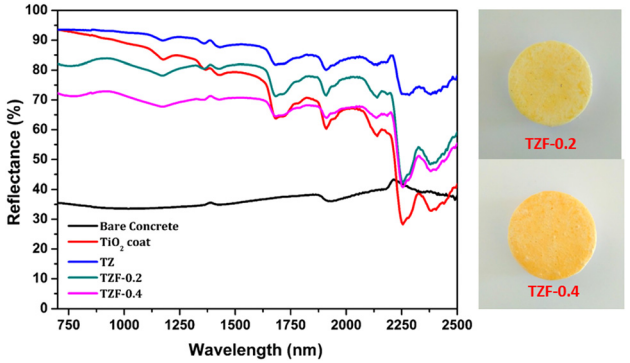

Fig. 17 NIR reflectance spectra of coated TZ, TZF-0.2 and TZF-0.4 in comparison with TiO_2 and bare concrete coatings.

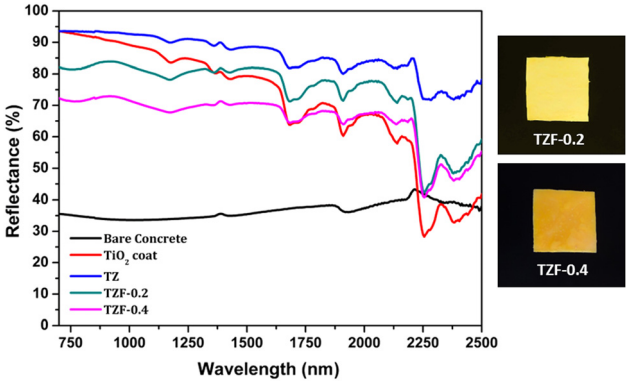

Fig. 19 NIR reflectance spectra of coated TZ, TZF-0.2 and TZF-0.4 in comparison with the TiO_2 coating and bare Al sheet.

Table 9 Percentage NIR reflectance, R^* values and CIE $L^*a^*b^*$ coordinates for the selected pigment coatings over concrete

Sample	R^* (%)	L^*	a^*	b^*
Concrete	34.94	61.911	0.055	3.952
TiO_2 coat	85.17	97.686	−0.221	0.473
TZ	89.31	96.532	0.006	4.085
TZC-0.2	76.28	95.283	−4.067	11.812
TZC-0.4	61.91	88.809	−3.294	14.894
TZF-0.2	79.38	85.127	4.797	18.588
TZF-0.4	69.26	85.768	4.98	26.445

Table 10 Percentage NIR reflectance, R^* values and CIE $L^*a^*b^*$ coordinates for the selected pigment coatings over an Al sheet

Sample	R^* (%)	L^*	a^*	b^*
Bare Al sheet	56.65	78.329	−0.12	0.995
TiO_2 coating	88.56	98.426	−0.443	0.59
TZ	94.20	99.285	−0.19	0.461
TZC-0.2	87.53	96.956	−1.279	4.76
TZC-0.4	58.65	91.099	−4.127	25.043
TZF-0.2	90.59	95.427	1.07	7.784
TZF-0.4	74.57	77.834	13.869	42.26

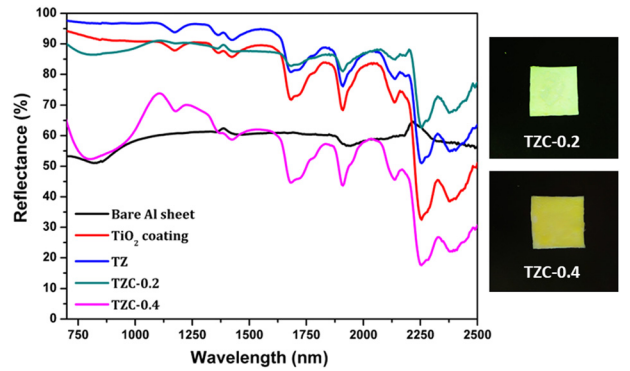

Fig. 18 NIR reflectance spectra of coated TZ, TZC-0.2 and TZC-0.4 in comparison with the TiO_2 coating and bare Al sheet.

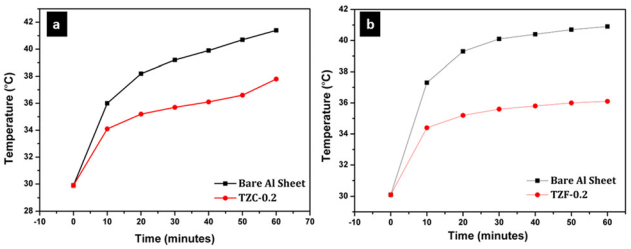

Fig. 20 Time dependent temperature measurements obtained for (a) TZC-0.2 and (b) TZF-0.2 coated Al sheet roofing along with the bare Al sheet.

for NIR reflecting pigments. So these compositions can be considered promising pigment candidates.

Chemical stability studies

The chemical stability of the developed pigments towards acid and alkaline environments was evaluated by treating them with 5% HNO_3 and 5% NaOH solutions. The resistance of the selected pigment compositions towards chemically aggressive environments was studied by weighing out 0.5 g of the pigment and then treating it with acid/alkaline solutions, accompanied by constant stirring. After 30 minutes, the pigment samples were collected by centrifugation, washed and dried. The dried powders were then subjected to chromatic studies to measure their CIE $L^*a^*b^*$ coordinates. The NIR reflectance of the pigments was also measured after acid/alkali treatment. The obtained CIE $L^*a^*b^*$ coordinates are listed in Table 11 along with the colour difference ΔE^* calculated. The XRD analysis of three selected pigment compositions was also carried out after chemical treatment. The XRD patterns obtained can be clearly indexed to the cubic $TiZn_2O_4$ phase and are exactly in agreement with the XRD patterns of untreated samples (Fig. S5, ESI†). Even after acid/alkali treatment, the pigments have retained their colour characteristics and NIR reflectance without significant changes. Thus, the developed $TiZn_2O_4$ based compositions are found to be resistant to harsh chemical environments, which makes them suitable for commercial application.

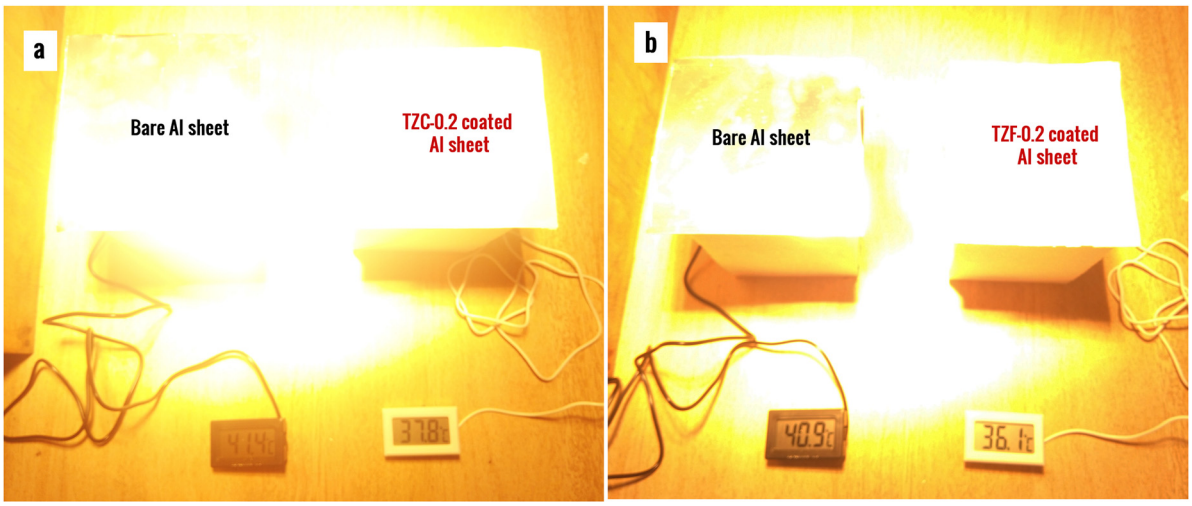

Fig. 21 Difference in interior temperatures observed after thermal shielding studies using (a) TZC-0.2 and (b) TZF-0.2 coated Al sheet roofing in comparison with bare Al sheet roofing.

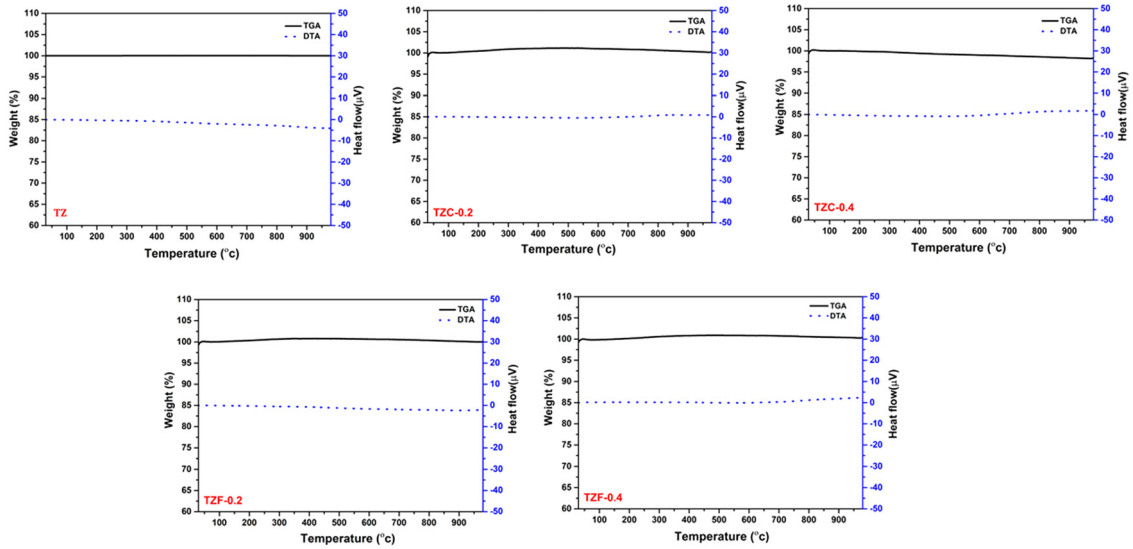

Fig. 22 TGA and DTA curves of TZ, TZC-0.2, TZC-0.4, TZF-0.2 and TZF-0.4 pigment powders.

Table 11 CIE $L^*a^*b^*$ coordinates, colour difference ΔE^* and percentage NIR reflectance obtained after acid/alkali treatment of the developed pigment samples

	Untreated				HNO_3					NaOH				
Sample	R^* (%)	L^*	a^*	b^*	R^* (%)	L^*	a^*	b^*	(ΔE^*)	R^* (%)	L^*	a^*	b^*	(ΔE^*)
TZ	96.76	98.41	−0.05	0.99	96.8	98.51	−0.22	1.26	0.33	95.63	97.03	0.33	2.72	2.24
TZC-0.2	62.83	91.12	−7.50	24.18	62.02	90.87	−7.48	24.27	0.27	61.25	90.59	−7.32	26.25	2.14
TZC-0.4	47.61	82.92	−5.48	36.41	47.34	83.02	−5.41	36.63	0.25	46.32	82.94	−4.65	36.92	0.98
TZF-0.2	87.81	84.81	6.92	31.72	86.82	84.90	6.56	30.88	0.93	83.73	83.20	7.43	31.99	1.71
TZF-0.4	77.83	73.70	14.49	37.78	77.25	72.93	15.09	38.15	1.05	76.45	72.76	14.92	37.36	1.12

Conclusion

Here $TiZn_2O_4$ based NIR reflecting inorganic pigments which are economically affordable and eco-friendly were developed through a citric acid fuel-assisted solution combustion strategy. The optical properties of the inverse spinel structured $TiZn_2O_4$ lattice were modified with the incorporation of Cu^{2+} and Fe^{3+} ions as chromophores capable of imparting attractive hues and

reducing band gaps. The replacement of octahedral Zn^{2+} ions by Cu^{2+} and Fe^{3+} ions in varying amounts resulted in a series of pigment colours ranging from greenish-yellow to reddish-brown. The resulted crystal structures were characterised well and site allocations and lattice changes were understood in detail with the help of Rietveld refinement of XRD patterns. Four among the ten developed compositions were selected for application as possible NIR reflecting pigments. They exhibited percentage NIR reflectance ranging from 47.61 to 87.81% and showed very high thermal and chemical stability. Pure $TiZn_2O_4$ showed a very high NIR reflectance of 96.76% which is comparable with those of commercial TiO_2 pigments. The thermal shielding studies conducted using two of the selected pigment candidates showed a reduction in interior temperature by 3.6 °C for Cu^{2+} doped $TiZn_2O_4$ and 4.8 °C for Fe^{3+} doped $TiZn_2O_4$ coated roofing relative to uncoated roofed interiors. Thus Cu^{2+} and Fe^{3+} doped $TiZn_2O_4$ pigments can ensure better thermal conditioning of buildings with zero cost to the environment. Apart from tackling the urban heat island effect, these pigments have the capability for energy conservation over the long term. Further modifications of the $TiZn_2O_4$ lattice with suitable dopants and synthetic strategies may result in pigments with enhanced optical and solar reflectance properties.

Conflicts of interest

There are no conflicts to declare.

Acknowledgements

DJ thanks the University Grants Commission, Government of India for the Senior Research Fellowship. CPJ acknowledges DSKPDF for financial support.

References

1 G. Pfaff, *Inorganic pigments*, de Gruyter, 2017.
2 J. G. Speight, in *Environmental Inorganic Chemistry for Engineers*, ed. J. G. Speight, Butterworth-Heinemann, 2017, pp. 111–169, DOI: 10.1016/B978-0-12-849891-0.00003-5.
3 G. Gramm, G. Fuhrmann, M. Wieser, H. Schottenberger and H. Huppertz, *Dyes Pigm.*, 2019, **160**, 9–15.
4 S. Divya and S. Das, *Ceram. Int.*, 2021, **47**, 30381–30390.
5 M. Kato, M. Takahashi, H. Unuma and S. Suzuki, *J. Ceram. Soc. Jpn.*, 1999, **107**, 181–183.
6 J.-L. Wang, Y.-Q. Li, Y.-J. Byon, S.-G. Mei and G.-L. Zhang, *Powder Technol.*, 2013, **235**, 303–306.
7 A. Eroles and A. Friedberg, *J. Am. Ceram. Soc.*, 1965, **48**, 223–227.
8 M. Heck, T. Rehren and P. Hoffmann, *Archaeometry*, 2003, **45**, 33–44.
9 P. Wanrooij, U. Agarwal, J. Meuldijk, J. V. Kasteren and P. Lemstra, *J. Appl. Polym. Sci.*, 2006, **100**, 1024–1031.
10 K. White, T. Detherage, M. Verellen, J. Tully and M. P. S. Krekeler, *Environ. Earth Sci.*, 2014, **71**, 3517–3528.
11 H. Liu, K. Liu, H. Fu, R. Ji and X. Qu, *Environ. Pollut.*, 2020, **263**, 114484.
12 M. Jansen and H. P. Letschert, *Nature*, 2000, **404**, 980–982.
13 A. Coccato, L. Moens and P. Vandenabeele, *Heritage Sci.*, 2017, **5**, 1–25.
14 S. Jose, D. Joshy, S. B. Narendranath and P. Periyat, *Sol. Energy Mater. Sol. Cells*, 2019, **194**, 7–27.
15 P. K. Thejus, K. V. Krishnapriya and K. G. Nishanth, *Sol. Energy Mater. Sol. Cells*, 2021, **219**, 110778.
16 B. Sarkodie, C. Acheampong, B. Asinyo, X. Zhang and B. Tawiah, *Color Res. Appl.*, 2019, **44**, 396–410.
17 N. Noaa, 2019, www.ncdc.noaa.gov/sotc/global/201813.
18 H. Akbari, P. Berdahl, R. Levinson, S. Wiel, B. Miller and A. Desjarlais, *California Energy Commission PIER Program; Heat Island Group*, Lawrence Berkeley National Laboratory: Berkeley, CA, USA, 2006.
19 A. Synnefa, M. Santamouris and K. Apostolakis, *Sol. Energy*, 2007, **81**, 488–497.
20 R. Sharma, S. Tiwari and S. K. Tiwari, *ACS Sustainable Chem. Eng.*, 2018, **6**, 2004–2010.
21 R. L. Millard, R. C. Peterson and B. K. Hunter, *Am. Mineral.*, 1995, **80**, 885–896.
22 B. H. Toby, *J. Appl. Crystallogr.*, 2001, **34**, 210–213.
23 A. Marzo, P. Ferrada, F. Beiza, J. Alonso-Montesinos, J. Ballestrín and R. Román, *EuroSun*, 2016, *ISES Conference Proceedings*, 2016.
24 S. Souza, I. Santos, M. Silva, M. Cássia-Santos, L. Soledade, A. Souza, S. Lima and E. Longo, *J. Therm. Anal. Calorim.*, 2005, **79**, 451–454.
25 X. Lu, W. Bian, Y. Li, H. Zhu, Z. Fu and Q. Zhang, *J. Am. Ceram. Soc.*, 2018, **101**, 1646–1654.
26 J. K. Burdett, G. D. Price and S. L. Price, *J. Am. Chem. Soc.*, 1982, **104**, 92–95.
27 M. Arillo, M. López, C. Pico, M. Veiga, A. Jimenez-Lopez and E. Rodrıguez-Castellon, *J. Alloys Compd.*, 2001, **317**, 160–163.
28 C. Vinuthna, D. Ravinder, R. Madhusudan and D. Ravinder, *Int. J. Eng. Res. Appl.*, 2013, **3**, 654–660.
29 U. Steinike, P. Druska, B. Wallis, D.-C. Uecker and V. Sepelak, *Chem. Pap.*, 1998, **52**, 147–151.
30 S. Dhankhar, K. Gupta, G. Bhalerao, N. Shukla, M. Chandran, B. Francis, B. Tiwari, K. Baskar and S. Singh, *RSC Adv.*, 2015, **5**, 92549–92553.
31 J. Liu, M. Zeng and R. Yu, *Sci. Rep.*, 2016, **6**, 1–10.
32 T. Aghavnian, J.-B. Moussy, D. Stanescu, R. Belkhou, N. Jedrecy, H. Magnan, P. Ohresser, M.-A. Arrio, P. Sainctavit and A. Barbier, *J. Electron. Spectrosc. Relat. Phenom.*, 2015, **202**, 16–21.
33 R. Gupta and S. Sen, *Phys. Rev. B: Solid State*, 1974, **10**, 71.
34 N. McIntyre and D. Zetaruk, *Anal. Chem.*, 1977, **49**, 1521–1529.
35 J. Peoples, X. Li, Y. Lv, J. Qiu, Z. Huang and X. Ruan, *Int. J. Heat Mass Transfer*, 2019, **131**, 487–494.
36 S. L. Reddy, T. Endo and G. S. Reddy, *Adv. Aspects Spectrosc.*, 2012, 4–48.
37 L. I. Granone, K. Nikitin, A. Emeline, R. Dillert and D. W. Bahnemann, *Catalysts*, 2019, **9**, 434.
38 C. Ding, A. Han, M. Ye, Y. Zhang, L. Yao and J. Yang, *RSC Adv.*, 2018, **8**, 19690–19700.
39 P. Thejus and K. Nishanth, *Sol. Energy Mater. Sol. Cells*, 2019, **200**, 109999.